Origin, Composition and Relative Timing of Seaward Dipping Reflectors on the Pelotas Rifted Margin

Caroline Harkin [a*], Nick Kusznir [a], Alan Roberts [b], Gianreto Manatschal [c], Brian Horn [d]

[a] *Department of Earth, Ocean and Ecological Sciences, University of Liverpool, Liverpool, L69 3GP, U.K.*

[b] *Badley Geoscience Ltd, North Beck House, Spilsby, Lincolnshire, PE23 5NB, U.K. ORCID 0000-0003-4839-0741*

[c] *Institut de Physique du Globe de Strasbourg; CNRS-UMR 7516, Université de Strasbourg, 1 rue Blessig, F-67084 Strasbourg Cedex, France.*

[d] *ION, 31 Windsor Street, Chertsey, KT16 8AT, U.K.*

Corresponding Author Email: C.Harkin@liverpool.ac.uk

Keywords: seaward dipping reflectors, gravity inversion, rifted margin, Pelotas Basin

Abstract

The mechanism by which seaward dipping reflectors (SDRs) are formed is a topic of debate. Two contrasting models exist for their formation, the volcanic-faulting model and the volcanic-loading model. Each of these models has important implications for the processes which control the structure and formation of magma-rich rifted continental margins. We have examined high-quality deep-seismic reflection data across the Pelotas Basin, offshore Brazil. These data reveal a remarkable set of SDRs, for which we have investigated the likely nature of their formation. The total package of SDRs has an across-strike width of ~200 km and a variable vertical thickness of ~10-17 km, previously interpreted as volcanic flows.

Detailed observations, however, show changes in seismic character and geometry within the SDR package, which suggest a complex and varied evolution.

We have used gravity anomaly inversion and seismic observations together to investigate the likely composition of the SDRs by determining the proportion of basaltic material to sedimentary/volcaniclastic material (basalt fraction) within the SDRs. This has been achieved by minimising the difference between the depth of the gravity Moho and seismic Moho in order to quantify the lateral variation in basalt fraction, taken to be proportional to the bulk density of the package. The density of the SDR package together with seismic interpretation is then used to infer the composition, depositional environment, source and time of formation relative to breakup.

Our analysis suggests that the overall SDR basalt fraction and bulk density decrease oceanwards, possibly due a change in the type of volcanic deposits from predominantly subaerial to volcaniclastics, possibly deposited subaqueously. The SDRs can be split into three sub-packages. The two inner SDR packages are interpreted to consist of lava flows sourced from syn-tectonic, subaerial eruptions, associated with the onshore Paraná Large Igneous Province, flowing eastwards into an extensional basin. The outer SDR package shows reflector geometries that progressively offlap oceanwards, interpreted as extrusives sourced from an eastwards-migrating, newly formed ocean ridge. Our analysis suggests that both the volcanic-faulting and volcanic-loading models for SDR formation are applicable to the Pelotas rifted margin, recording distinct syn-rift and syn-breakup magmatic events. We show that both SDR formation models can be recognised in a naturally occurring example and can coexist on the same margin.

1. Introduction

Magma-rich rifted margins are typically associated with extensive amounts of magmatic addition to the crust, comprising extrusive lavas and intrusive dykes, sills and gabbroic

bodies. Magmatic extrusives commonly take the form of seaward dipping reflectors (SDRs), believed to result from the lateral migration and accretion of both subaerial and submarine lava flows during rifting, breakup and initial sea-floor spreading (e.g. Bodvarsson and Walker, 1964; Buck, 2017; Geoffroy, 2005; Hinz, 1981; Mutter et al., 1982). The formation and internal composition of SDRs has been generalised worldwide from a small number of well penetrations, localised onshore analogues and seismic studies (e.g. Geoffroy et al., 2001; Larsen and Saunders, 1998; McDermott et al., 2018; Mutter et al., 1982; Planke and Eldholm, 1994). As a result, two contrasting models exist for the formation of SDRs. In this paper we investigate whether either of these models can be applied to a spectacularly imaged set of SDRs, on the Pelotas margin, southern Brazil. To do so, we have used gravity inversion and seismic interpretation to investigate the composition, origin and timing (relative to breakup) of the Pelotas SDRs and have then interpreted the processes which led to their formation.

The term seaward dipping reflectors refers to a wedge of stacked, arcuate reflectors that dip seawards with increasing flow thickness down dip (Mutter et al., 1982). SDR wedges vary in size globally, but can reach several kilometres in vertical thickness and can extend laterally for hundreds of kilometres (Hinz et al., 1999; Mutter et al., 1982; White et al., 2008). Seismic velocities within SDR packages typically increase down-dip and commonly average ~5 km s^{-1} for the entire section (Mutter et al., 1982; White et al., 2008). Such velocities are compatible with an igneous origin, particularly basalt flows, leading to the assumption supported by limited well data and onshore analogues (Eldholm et al., 1989; Fitton et al., 2000; Larsen and Saunders, 1998; Planke and Cambray, 1998; Planke and Eldholm, 1994), that SDRs are composed predominantly of primary igneous material with minor associated deposits of tuffs, volcaniclastics and/or sedimentary material. The composition of SDRs worldwide is generally assumed to follow this premise, but with drilling expensive and SDRs often buried deep beneath sedimentary cover, the determination of actual SDR composition is often based only on seismic interpretation or observations from landward-flow equivalents. To

advance this basic understanding, we present here a new technique to investigate the composition of SDRs using both gravity anomaly and seismic reflection data.

Using wide-angle, high-quality seismic reflection data and gravity anomaly inversion, we examine SDRs on the Pelotas margin, Brazil to investigate whether they are composed predominantly of massive basaltic flows, sedimentary/volcaniclastic material, or a combination of both. By matching the Moho in both depth and two-way travel-time (TWTT) from gravity and seismic reflection data, we test the proportion of basaltic material to sedimentary/volcaniclastic material (the basalt fraction). The results are used to determine the lateral variation in basalt fraction within the SDRs, which parameterises the bulk density of the package. Interpretation of SDR composition and their associated environment of emplacement can then lead to an interpretation of the magmatic/depositional source and timing relative to breakup. From this, we can assess the applicability of existing models for SDR formation to the Pelotas example. We use the joint inversion of gravity and seismic Moho results to test our approach and investigate the combined density of the SDR package and basement, comparing it against laterally varying basalt fraction results.

1.1 Previous models for the formation of seaward dipping reflectors

SDRs are believed to form from intense volcanic activity during rifting and breakup (Buck, 2017; Hinz, 1981; Mutter et al., 1982; Paton et al., 2017) and are often related to the formation of large igneous provinces (LIPs) (Buck, 2017). Their basic structure consists of a series of stacked flows forming a wedge with an angle of dip that increases with depth.

On the Outer Vøring Plateau (offshore Norway), Hinz (1981) showed that the seismic velocities of such flows vary from 3-4 km s^{-1} in the upper section of the wedge to 5 km s^{-1} in the lower section of the wedge. Similarly, also on the Outer Vøring Plateau, Mutter et al. (1982) and Talwani et al. (1981) derived an average velocity of 4.8 km s^{-1} across a set of SDRs for which the total range in velocity is 2.6 km s^{-1} to 6.4 km s^{-1}. Within the SDRs of the Faroes

margin (NE Atlantic), White et al. (2008) noted a marked decrease in velocity at the base of the flows (~4.2-4.5 km s^{-1},), while the average seismic velocity of the entire wedge is ~5 km s^{-1}. These seismic studies, together with sparse well data predominantly from Iceland, Greenland and the Norwegian Sea (Eldholm et al., 1987; Larsen and Saunders, 1998; Parons et al., 1989; Planke and Eldholm, 1994; Viereck et al., 1989), have led to the general conclusion that SDRs are composed predominantly of volcanic material with localised interbedded deposits of volcaniclastic/sedimentary material.

Two different models for SDR formation exist within the literature. One suggests that the flows are formed subaerially on continental crust during fault-controlled extension prior to continental breakup, sourced from intrusive dykes (Geoffroy, 2005; Hinz, 1981; Paton et al., 2017; Quirk et al., 2014). The other also suggests that the flows are erupted subaerially and

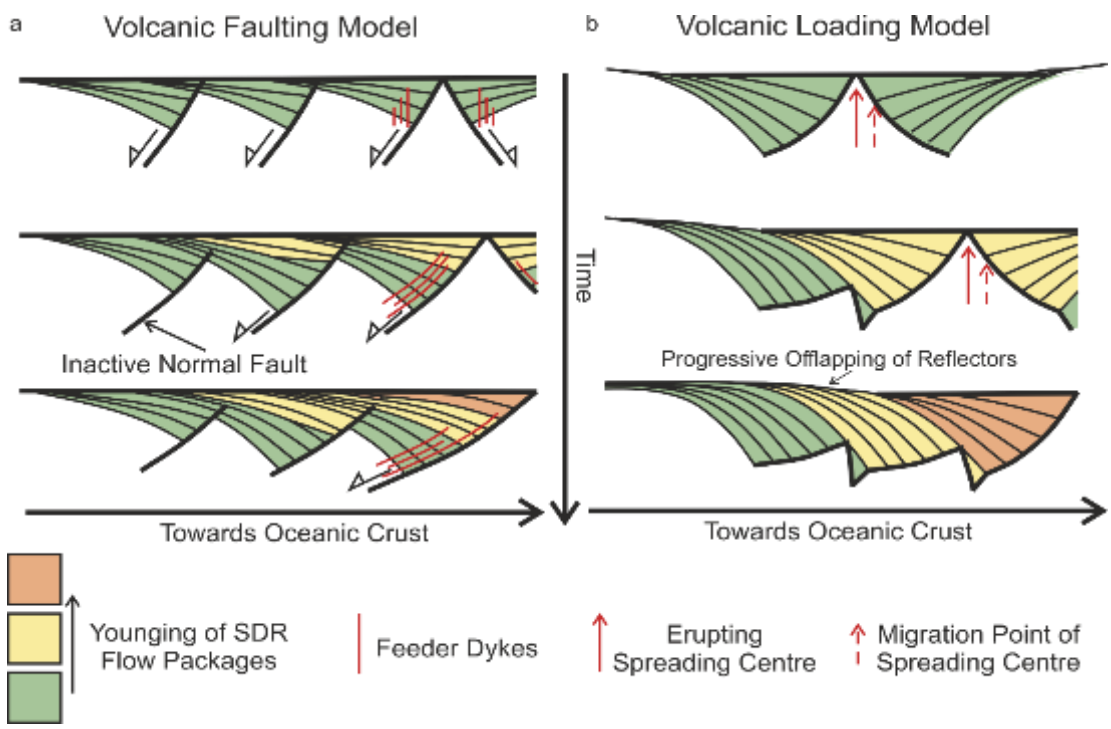

Figure 1. Cartoon summary of models for SDR formation (after Buck, 2017). a) Volcanic faulting model where large normal faults that dip towards the continent are intruded by dykes (SDR source) that fill the half-grabens with extrusive volcanic material. These faults progressively rotate and become inactive as younger faults are generated in an oceanwards direction. b) Volcanic loading model where a spreading centre erupts lava subaerially, forming successions of flows that dip towards the spreading centre. Migration of the spreading centre leads to a stacking of the SDR packages towards the oceanic crust.

sourced from dykes, but contrastingly they are considered to form through loading and subsidence, forming the uppermost layers of oceanic crust at the initiation of seafloor spreading (Bodvarsson and Walker, 1964; Mutter et al., 1982; Talwani et al., 1981). Following the terminology used by Buck (2017) we call these models the volcanic-faulting model and the volcanic-loading model respectively (Fig. 1). Barton & White (1997), have previously suggested both types of SDRs exist on the Rockall Atlantic margin (Barton and White, 1997), while McDermott et al. (2018) interpret both types of SDR in the Pelotas Basin.

The volcanic-faulting model for SDR formation (Fig. 1a) invokes large landward-dipping normal faults, within continental crust, as the main mechanism for forming a large volume of accommodation space which then fills with extrusive basalt flows (Barton and White, 1997; Buck, 2017; Geoffroy, 2005; Geoffroy et al., 2001; Gibson and Love, 1989; Quirk et al., 2014). Using seismic reflection and well data from the Vøring Plateau (ODP Site 642), Eldholm et al. (1989) and Gibson & Love (1989) suggested that the observed SDR sequence formed by normal fault extension within continental crust. This work showed that the Vøring Plateau SDRs consist of subaerial tholeiitic basalt flows with a high silica content resulting from continental crustal contamination. They also contain xenoliths of gneiss and quartz-mica schist, implying the underlying basement comprises continental crust. These flows exhibit a low proportion of dykes relative to the flow volume, but it is suggested that SDR formation occurred predominantly by lava flowing onto continental crust from feeder dykes intruded along normal fault planes, which subsequently rotated to a low angle (Eldholm et al., 1989; Meyer et al., 2007). The SDR structure should therefore consist of a thick inclined pile of lava flows underlain by a sheeted dyke complex and a fault surface. Later studies (Geoffroy, 2005; Geoffroy et al., 2001), have also used the same mechanism and process to explain SDR formation.

The volcanic-loading model (Fig. 1b) originated from onshore observations of dyke-fed volcanic flows in Iceland, that dip towards volcanic centres at ~5-10° and also thicken down-dip (Palmason, 1973; Palmason and Saemundsson, 1974; Walker, 1960, 1959). Subsidence, as a result of the successive loading of the flows, was recognised as the cause for their increasing dip (Walker, 1960). A kinematic model for the emplacement of the flows was developed by Bodvarsson and Walker (1964), in which isostatically-compensated lava flows are fed by dykes at a spreading centre. Subsequent studies have used the volcanic-loading model to explain the formation of SDRs as coincident with sea-floor spreading in areas such as East Greenland, the Voring Plateau and the South Atlantic (Lenoir et al., 2003; Morgan and Watts, 2018; Mutter et al., 1982; Paton et al., 2017; Pindell et al., 2014; Talwani et al., 1981).

Both SDR formation models result in inclined piles of lava flows but can often be distinguished by the relationship of individual SDR reflectors. SDRs formed by subsidence and loading will display progressive offlapping in the direction of ridge migration, while SDRs formed by faulting should show offsets, particularly at the base of the flows. Here we investigate if either of these formation models for SDRs are applicable to the SDRs observed in the Pelotas Basin.

1.2 The opening of the South Atlantic Ocean and the formation of the Paraná-Etendeka province

This study investigates a regional seismic line from the Pelotas Basin, offshore Brazil that lies on the Arc de Torres (Fig. 2). Offshore southern Brazil comprises several basins; the Esperito-Santo Basin, the Campos Basin, the Santos Basin and the Pelotas Basin (Fig. 2a, Stica et al., 2014). Typical magma-poor features dominate the northern basins (Esperito-Santo and Campos), while large amounts of volcanism typical of magma-rich margins, dominate in the southern basins (Santos and Pelotas) (Stica et al., 2014). Namibia is often cited as the conjugate margin to the Pelotas Basin (Blaich et al., 2013; Gladczenko et al., 1997). However,

plate reconstructions and potential field data (Graça, 2018; Heine et al., 2013) suggest the conjugate to the Pelotas Basin could instead be the Western Rio Grande Rise, a small continental block forming part of the Rio Grande Rise situated east of the Pelotas Basin (Fioravanti, 2014)(Fig. 2a).

Formation of the South Atlantic Ocean resulted from the breakup of the South American and African plates as part of Gondwana during the Late Jurassic and Early Cretaceous. Diachronous breakup occurred from south to north, with the oldest breakup in the southern South Atlantic recorded at ~138 Ma, continuing through to ~115 Ma in the northern South Atlantic (Pérez-Diaz and Eagles, 2014). Breakup for the Pelotas Basin is dated using magnetic anomaly M4 at ~127 Ma (Gradstein et al., 1994; Hawkesworth et al., 2000) while sedimentary material displays evidence for rifting on the Brazilian margin as early as 140 Ma (Chang et al., 1992).

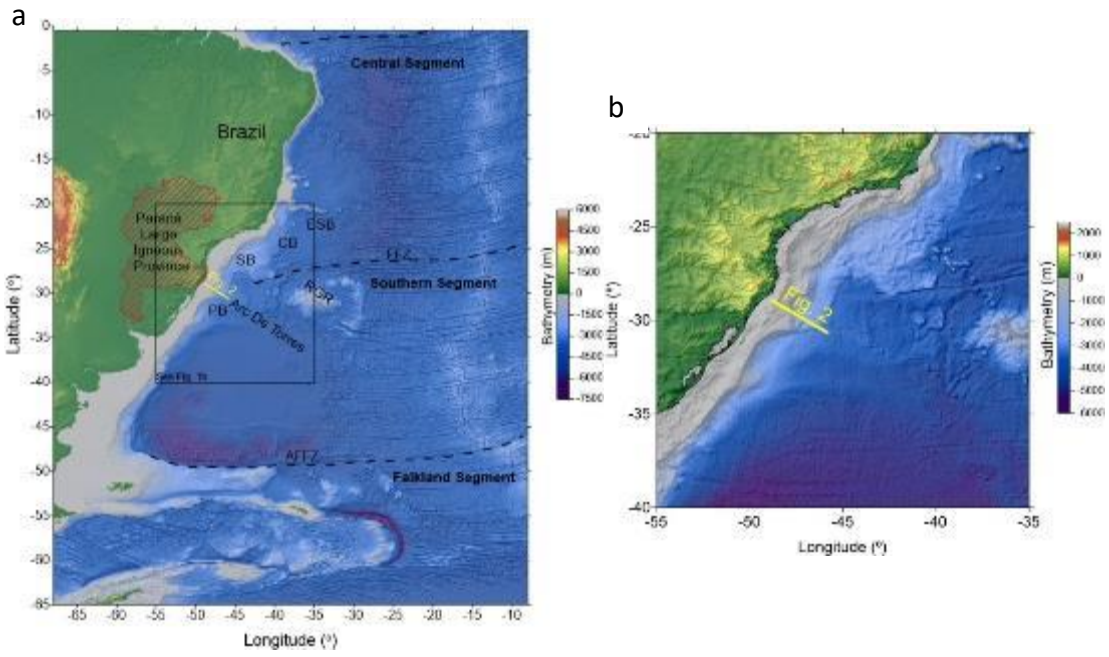

Figure 2. a) Bathymetric/topographic map of the South Atlantic on the western side of the Mid-Atlantic Ridge, with an overlay of shaded-relief free-air gravity anomaly. ESB, Esperito-Santo Basin; CB, Campos Basin; SB, Santos Basin; PB, Pelotas Basin; AFFZ, Agulhas-Falkland Fracture Zone; FFZ, Florianopolis Fracture Zone; RGR, Rio Grande Rise. Note location of seismic line (Fig. 3) in relation to Paraná LIP and Arc De Torres. b) Enlargement of box shown in (a), location of seismic profile shown in Fig. 3.

The formation of the Paraná-Etendeka LIP (Fig. 2a) is believed to be related to the breakup of Gondwana. The Paraná-Etendeka LIP covers an estimated area of $1.2x10^6$ km^2 in both South America and Africa, with additional offshore deposits (Hawkesworth et al., 1992). Onshore deposits in South America reach the coastline at one location in the Pelotas Basin, where the seismic line is situated. There is a major geographic asymmetry in the Paraná-Etendeka LIP, with ~95% of the rocks preserved on the South American plate (Paraná). The majority of the extrusives have been identified as tholeiitic basalts with subsidiary deposits of rhyolites, rhyodacites and andesites (Hawkesworth et al., 2000; Peate et al., 1992; Renne et al., 1996; Stica et al., 2014).

The main eruption period of the Paraná-Etendeka LIP is believed to have occurred within a relatively short time-period of <2 Myr, with early ages recorded at ~133 Ma for Paraná basalts and ~131 Ma for the Ponta Grossa dyke swarm located in the northern region of the Paraná (Janasi et al., 2011; Renne et al., 1996; Thiede and Vasconcelos, 2010). Peak activity of the Paraná has been identified between 133-130 Ma with related volcanism continuing until 124 Ma (Hawkesworth et al., 2000). Paraná magmatism, in particular the orientation of dyke swarms, is believed to be related to extension associated with the opening of the South Atlantic Ocean (Renne et al., 1996; Turner et al., 1994).

2. Seismic observations

A wide-angle, long-offset seismic-reflection line from the Pelotas Basin (courtesy of ION Geophysical) has been used to establish a seismic interpretation that can be used as the basis for subsequent quantitative modelling and analysis (Fig. 3). A previous seismic interpretation of this line was carried out by Stica et al. (see fig. 6, 2014) and McDermott et al. (2018). An un-interpreted seismic reflection cross section can be obtained from ION Geophysical at https://www.iongeo.com/content/documents/Resource%20Center/Brochures%20and%20Data%20Sheets/Data%20Sheets/Data%20Library/DS_GEO_PelotasSPAN.pdf. No seismic refraction data are available for this area.

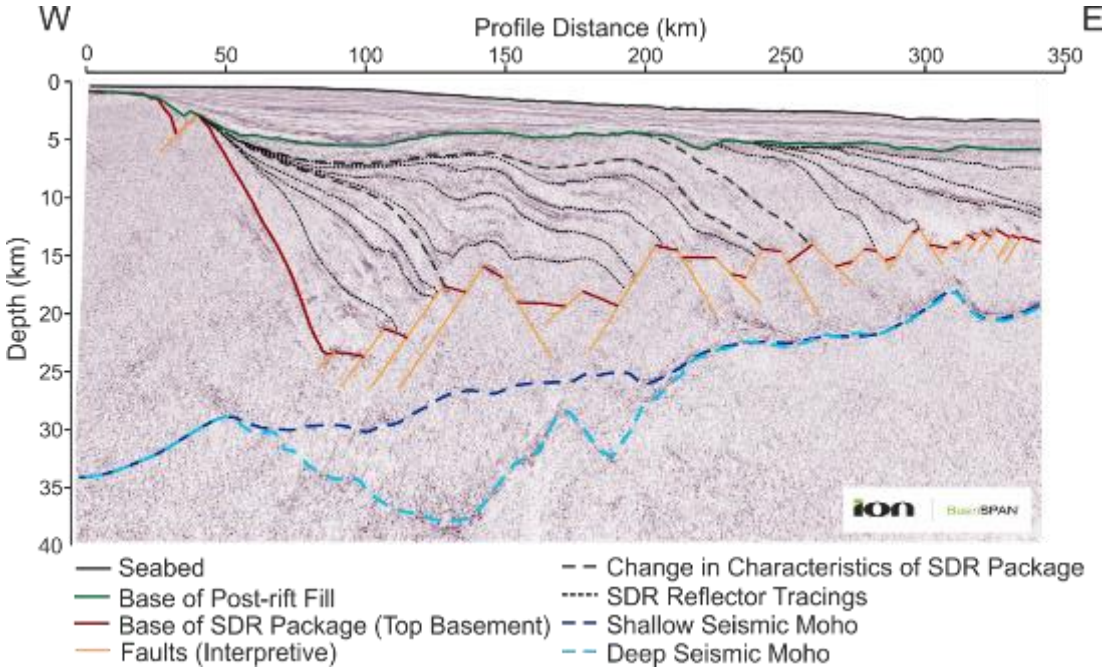

Figure 3. Seismic interpretation of Pelotas PSDM seismic profile, see Fig. 2 for location.

The pre-stack depth-migrated (PSDM) seismic profile has allowed us to interpret the geological boundaries of top basement and seismic Moho (Fig. 3). When interpreting the seismic Moho, we look for a deep continuous reflector, of which there are two possible candidates (see discussion below). For top basement we take the base of the sediment fill and extrusive magmatic material (SDRs). We have also interpreted the base of the post-rift sediment fill above the SDR package, defining a base-sediment/top-SDR surface.

At the proximal margin, top basement is sub-horizontal at a shallow depth of ~500 m, passing eastwards into a more steeply-dipping surface (~25°) which reaches a maximum depth of ~23 km at line coordinate ~90 km. The top basement surface then follows an interpreted series of normal faults, which define a set of horst and graben structures across most of the profile (see also Stica et al., 2014, fig. 6). These structures shallow oceanwards from a depth of ~23 km to ~14 km (Fig. 3). Within the basement there is a lack of reflectivity which would suggest the presence of dykes, although dykes could be present along the dipping faults that make up the horst and graben top basement surface. However, if the SDRs formed via dykes from below the SDR package we then have to consider how the magma is able to travel up-dip, as there is a dip surface of ~25° inboard of the innermost SDRs. The lack of faults within the SDR package suggests they were not disturbed during or after formation so the dip surface must have been present prior to their occurrence. As a result, an alternative source for the SDRs should be considered. Between the base of the post-rift sediments and the top basement is the package of seaward dipping reflectors which have previously been interpreted as volcanic flows by Stica et al. (2014). A lateral change in first-order SDR geometry occurs at line-coordinate ~200 km, west of which proximal reflectors appear (in 2D) to originate from a single-point source, while to the east, reflectors appear to migrate laterally towards the eastern end of the profile (Fig. 3).

Within the proximal SDRs two further separate packages can be seen (Fig. 3). The innermost reflectors have a single point of origin (at ~55 km) and extend across a distance of ~50 km as relatively smooth reflectors forming a wedge. These reflectors are also the deepest, reaching a depth of ~23 km. Immediately outboard and stratigraphically above, another set of proximal SDR reflectors (at a line-distance of 60-210 km) are more laterally extensive (~150 km), with an undulating geometry over the underlying top-basement horst and graben structure (Fig. 3). This package also originates from a single-point source in the west, close to that of the innermost SDRs, but the reflectors reach a shallower maximum depth of ~17 km.

The uppermost oceanward SDRs progressively offlap eastwards towards the end of the profile, forming relatively sub-parallel flows dipping at ~5° and thickening down-dip. The oceanward SDRs are ~10 km thick with individual reflectors extending across ~75 km. Separating the proximal and oceanward SDRs is a transitional package with weak internal reflectivity and a seismically-discontinuous upper surface.

On Figure 3, there are two reflectors which are possible seismic Moho candidates. One, the shallow seismic Moho, is interpreted approximately parallel to the top basement surface below the proximal SDRs, shallowing as top basement shallows. The other, the deep seismic Moho, lies deep below the proximal SDRs, reaching a maximum depth of 39 km (Fig. 3) before sharply rising to meet the shallow seismic Moho at a line-distance of 210 km and a depth of 24 km. Both candidates for seismic Moho then follow a strong reflector oceanwards, approximately 6 km below the top basement surface. We determine which reflector is the most realistic seismic Moho through the use of quantitative analyses.

3. Gravity inversion to determine Moho depth

At rifted margins, gravity inversion can be used to estimate the depth to the Moho and lithosphere thinning factor. The gravity inversion follows a methodology which is previously published, tried and tested by Greenhalgh & Kusznir (2007), Chappell & Kusznir (2008a), Alvey et al. (2008), Cowie et al. (2015), Roberts et al. (2018), Steinberg et al. (2018), Gozzard et al. (2018), Kusznir et al (2018), Alvey et al. (2018) and Harkin et al. (2019). Input requirements for the gravity inversion are bathymetry (Smith and Sandwell, 1997), satellite-derived free-air gravity anomaly (Sandwell and Smith, 2009), ocean-age isochrons (Müller et al., 1997) and sediment thickness information from seismic reflection data. First within the gravity inversion, the free-air gravity anomaly (g_{fag}) is corrected for the signals from bathymetry (g_b), sediment thickness (g_s) and lithosphere thermal effects (g_t) to calculate the mantle residual gravity anomaly (g_{mra}), where the density for seawater is taken as 1039 kg m^{-}

^{3} (Nayar et al., 2016), and the density of the mantle is 3300 kg m^{-3} (Jordan and Anderson, 1974). We take 2850 kg m^{-3} as the density for crustal material based on seismic velocity analysis, drilling results and laboratory experiments from Carlson and Herrick (1990) and Christensen and Mooney (1995). Constant basement and mantle densities are required to overcome non-uniqueness using Smith's Theorem (Smith, 1961).

$$g_{mra} = g_{fag} - g_b - g_s - g_t \quad (1)$$

The mantle residual anomaly is then filtered to remove high-frequency components using a Butterworth filter with a cut-off of 100 km. Using a 3D spectral inversion (Parker 1972), we invert the mantle residual gravity anomaly for Moho topography and in turn crustal thickness, assuming that the entire signal comes from variations in Moho depth. The incorporation of Smith's Theorem (Smith, 1961) allows us to provide a unique solution for any given set of input parameters given that the source density remains constant, the source is of finite extent and any vertical line does not pass through the source more than once. Iteration of the inversion gives an estimation of the lithosphere thinning factor, which is dependent upon the choice of decompression-melt parameterisation.

During rifting and breakup, magmatic material may be added to the crust in the form of extrusives and intrusives. Here we define breakup as the rupture and separation of continental crust and lithosphere (Tugend et al., 2018) and we define crust as crystalline basement. We estimate the thickness of this magmatic addition using a parameterisation of the decompression melting model of McKenzie & Bickle (1988) and White & McKenzie (1989), which is in turn dependent upon the lithosphere thinning factor calculated from the gravity inversion. The lithosphere thinning factor (γ) is defined as:

$$\gamma = 1 - \frac{1}{\beta}$$

(2)

Where β is the lithosphere stretching factor (McKenzie 1978).

The proximity of the Paraná LIP to the seismic line could have resulted in elevated mantle temperatures, producing a larger volume and thickness of decompression melting in excess of the average 7 km (White et al., 1992). In this study, we use a melting parameterisation that is representative of an end-member magma-rich margin, where decompression melting is expected to produce 10 km thick oceanic crust when maximum thinning is reached (γ = 1.0), with the onset of decompression melting occurring at γ = 0.5 (Chappell and Kusznir, 2008a). Parameterisation of decompression melting is discussed in more detail in Chappell & Kusznir (2008a) and Kusznir et al. (2018), with alternate solutions for modelling other types of rifted margins. For the Pelotas profile, Moho sensitivity to alternative magmatic parameterisations has no significant effect on the position of the Moho. We have therefore continued to use a magma-rich parameterisation for calculation of Moho depth. Magmatic parameterisation would become important if we wished to derive estimates of thinning factor and continental-crustal-basement thickness along the profile, for which knowledge of the magmatic thickness is required (Chappell and Kusznir, 2008a; Kusznir et al., 2018).

3.1 Initial gravity inversion results

Gravity inversion can be used to determine Moho depth across the section. We use it initially to predict Moho depth for two end-member scenarios for the composition of the SDR package (Fig. 4).

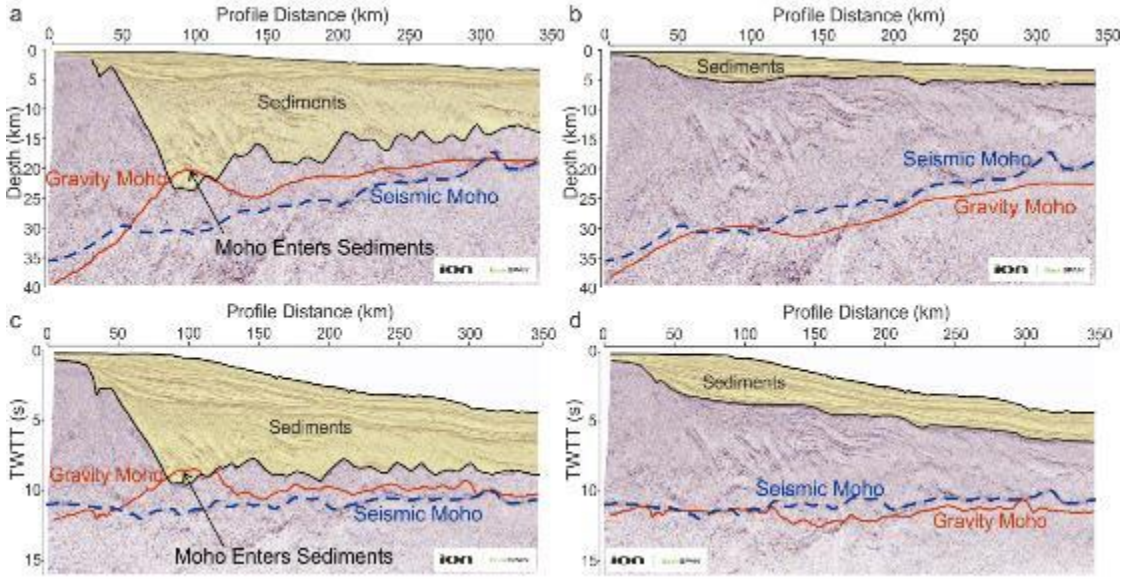

Figure 4. Testing end member scenarios for SDR package composition using gravity inversion. a) Gravity inversion Moho (red) and seismic Moho (blue) in depth resulting from modelling SDR package as sedimentary. Note the gravity inversion Moho inadmissibly entering the overlying sediments. b) Gravity inversion Moho (red) and seismic Moho (blue) in depth resulting from modelling SDR package as entirely basalt, with an equivalent density to basement. c) Gravity inversion Moho (red) and seismic Moho (blue) in time resulting from modelling SDR package as sedimentary. Note the gravity inversion Moho inadmissibly entering the overlying sediments. d) Gravity inversion Moho (red) and seismic Moho (blue) in time resulting from modelling SDR package as entirely basalt, with an equivalent density to basement.

The first end-member scenario (Fig. 4a, c), models the SDR package as entirely compaction-controlled sedimentary material. This corresponds to a top basement surface located at the base of the SDR package (Fig. 4a). The second end-member scenario (Fig. 4b, d), models the SDR package as entirely incompactable basaltic material, with the top basement surface effectively located at the top of the SDR package (Fig. 4b). For both end-member scenarios (Fig. 4), the gravity inversion Moho does not consistently match with either seismic Moho candidate. In the sedimentary end-member (Fig. 4a, c), the gravity inversion Moho is too shallow when compared against the seismic Moho, while in the basaltic end-member

scenario (Fig. 4b, d), the gravity inversion Moho matches the seismic Moho in the proximal domain but it too shallow within the distal domain. Additionally, for the sedimentary SDR package scenario a non-physical solution is produced where the gravity inversion Moho rises up into the deepest part of the SDR package (Fig. 4a). On the basis of the initial two gravity inversion results, the SDR package composition is likely to be neither fully sedimentary nor fully basaltic.

Uncertainties within the velocity model used for depth conversion below the SDR package can lead to uncertainties within the results using the PSDM seismic profile. Conversion of the gravity inversion Mohos into the time domain (PSTM profile), by assigning a velocity of 6.31 km s^{-1} to a basement density of 2850 kg m^{-3} (Birch, 1964) eliminates any depth-conversion uncertainties. Time domain results (Fig. 4c, d) once again show a mismatch between the gravity Moho for each scenario and the possible seismic Moho reflectors, as well as a non-physical solution for the sedimentary SDR package end-member.

Our initial results (Fig. 4) in both depth and time suggest that the SDR package is most likely to be a combination of both sedimentary and basaltic material, intermediate between the two end-member cases.

4. A test of SDR package density using joint inversion of gravity and seismic Mohos

We can test the combined density of the SDR package and the basement by combining our gravity inversion results and our seismic observations. To achieve this, we use joint inversion of the gravity Moho and the time seismic-reflection Moho (Cowie et al., 2016; Harkin et al., 2019). By comparing the gravity inversion Moho and the seismic Moho in the time domain (Fig. 5a), we can calculate the implied lateral variations in the average density of the basement. For the purposes of this test we include the SDRs within the basement (this is equivalent to the case of Fig. 4d). We initially use the shallow seismic Moho candidate within the joint inversion as the deep seismic Moho candidate lies at 14 s TWTT, which is much

deeper than the Moho guide of Warner (1987). Joint inversion results using the deep seismic Moho candidate are discussed later within the section.

Within the joint inversion we solve for the density and seismic velocity of the basement, allowing for their lateral variation that results in the gravity Moho matching the seismic Moho in the time domain. We use a linear Nafe-Drake relationship (Ludwig et al., 1970) to link basement density and seismic velocity together, as it fits with average oceanic crust seismic

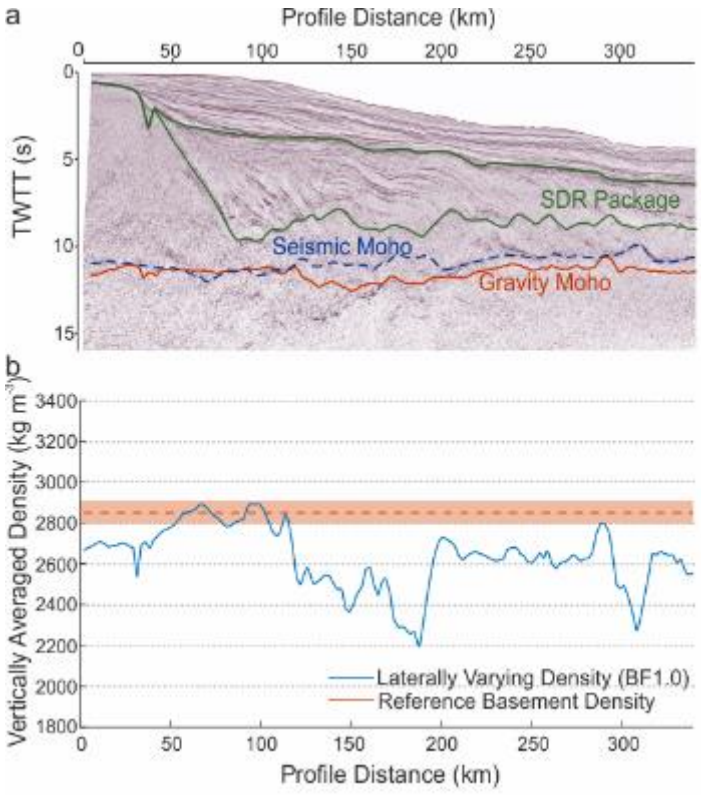

Figure 5. Joint inversion of seismic and gravity Mohos, providing an independent test of combined SDR and basement density. a) TWTT seismic section with shallow seismic Moho candidate (blue) and gravity inversion Moho (red) used in the joint inversion. b) Lateral variation in average basement density resulting from joint inversion using gravity inversion Moho (blue), compared against the initial basement density of 2850 kg m^{-3} (orange), with upper and lower bounds for typical crustal basement also shown (2800-2900 kg m^{-3}).

velocity and density measurements (Carlson and Herrick, 1990; Harkin, 2019; White et al., 1992). The lateral variation of basement density affects the depth of the Moho predicted from gravity inversion, while the lateral variation of basement seismic velocity affects the

conversion of the gravity inversion Moho from the depth to the time domain. The joint inversion requires an iterative adjustment of both basement density and seismic velocity until convergence is achieved. The advantage of this approach is that it avoids the seismic velocity uncertainties from the basement in the depth seismic reflection section.

The lateral variation in combined basement and SDR density is shown in Figure 5. This density, calculated from joint inversion, is the vertically averaged density between top SDRs and the shallow seismic Moho candidate. Figure 5b shows a significant lateral variation in this density and a deviation from 2850 kg m^{-3}, which is the initial density assumed for basement in the gravity inversion. Changing this initial basement density affects the absolute value of the joint inversion densities but does not change the pattern seen in the lateral variation.

Between a line-distance of 60 and 120 km (Fig. 5b), the density between top SDRs and seismic Moho from the joint inversion is high and similar to the initial density of 2850 kg m^{-3} assumed for basement. Further outboard, between 120 and 190 km, this density decreases substantially. At 190 km the density increases but does not reach the assumed value for basement. We interpret this lateral variation in the vertically averaged density between top SDRs and seismic Moho as indicating a lateral variation in the density of the SDR package. We believe this is more likely than the alternative, which is significant lateral variation in the density of the basement.

For the deep seismic Moho candidate, the joint inversion results show an average density in excess of 3000 kg m^{-3} across the proximal SDRs, which is more akin to mantle densities than basement and SDR densities.

5. Gravity inversion with basalt fraction

Initial gravity inversion results (Fig. 4) show that the SDR package is likely to comprise basaltic material interbedded with compactable sediments/volcaniclastics, but the proportion of

each is initially unknown. The joint inversion of gravity and seismic data also shows a lateral variation in SDR density. To investigate this further we have explored how varying the proportion of basaltic to sedimentary/volcaniclastic material, the basalt fraction, affects the Moho depth predicted by gravity inversion.

We define the basalt fraction (BF) as the proportion of basaltic material to sedimentary/volcaniclastic material, given as a fraction between 0 and 1. The calculated combined density of basalt and compaction-controlled sedimentary/volcaniclastic material is then used within the gravity inversion. Gravity inversions with four basalt fractions at intervals of 0.333 were computed (Fig. 6). For example, a basalt fraction of 0.333 represents a mixture of 33% basaltic material and 66% sedimentary/volcaniclastic material.

For the sediment component, we assume the sediments are composed of grains plus fluid in order to estimate bulk density. Using parameters from Sclater and Christie (1980), we estimate bulk density assuming a shaly-sand composition that compacts with depth. We modify this density profile to accommodate the inclusion of a basalt-sediment mix. Firstly, an empirical porosity-depth relationship (Athy, 1930) is assumed:

$$\phi(z) = \phi_0 e^{-cz}, \quad (3)$$

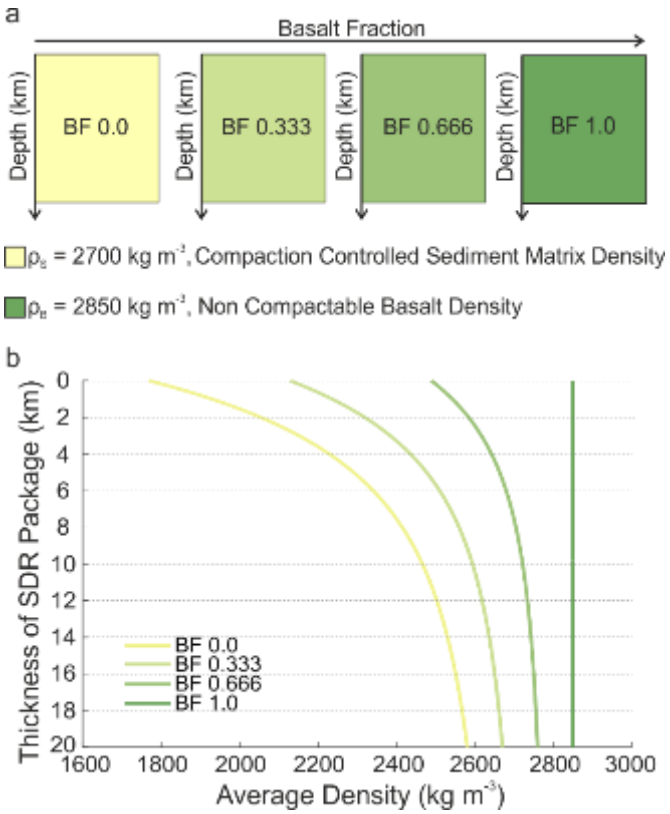

Figure 6. The basalt fraction. a) Schematic diagram illustrating the principle of the basalt fraction where a darkening in the colour of the box represents an increase in the proportion of basaltic material (i.e. bulk density). The proportion of sedimentary material to basaltic material is kept constant over all depths. b) Average density of SDR package over entire package thickness, given for each basalt fraction used within the gravity inversion, BF0.0, BF0.333, BF0.666, BF1.0. Densities are displayed for the case where top of SDR package (0 km) is at the seabed.

Where ϕ is porosity, ϕ_0 is surface porosity, c is the reciprocal of compaction length and z is the depth below the sediment surface (Sclater and Christie, 1980). This approximation leads to a bulk density relationship:

$$\rho = \phi\rho_w + (1-\phi)\rho_{mat}\,, \tag{4}$$

where ρ_{mat} is the matrix density and ρ_w is pore fluid density (Chappell and Kusznir, 2008b). Integration over depth gives average density as a function of depth:

$$\rho_{avg} = \rho_{mat} + \frac{\phi_0(\rho_{mat} - \rho_w)(e^{-cz}-1)}{cz},$$

391 *(5)*

392 Alteration of equation (5) to include the presence of a layer of mixed basalt and sedimentary
393 material then gives the following density-depth relationship:

394 $$\rho_{avg} = \left[\rho_{mat} + \frac{\phi_0(\rho_{mat} - \rho_w)(e^{-cz} - 1)}{cz}(1 - BF)\right] + BF.\rho_b \,,$$

395 *(6)*

396 in which *BF* is the basalt fraction and ρ_b is the density of basalt.

397 We assume that the density of basalt is 2850 kg m^{-3} (Moore, 2001) with 0% porosity, i.e. it is
398 non-compactable. For the sedimentary material all compaction parameters follow those
399 detailed in Sclater & Christie (1980), where for shaly-sand sediments, matrix density is given
400 as 2680 kg m^{-3} (rounded here to 2700 kg m^{-3}), surface porosity is 56% and c is 0.39 km^{-1}.

401 ## 5.1 Moho depths from gravity inversion with sensitivity to basalt fraction

402 The proportion of sedimentary to basaltic material has been investigated using a range of
403 basalt fraction values. Figure 7a shows Moho depths calculated from gravity inversion for
404 basalt fractions from 0 to 1, with a 0.333 interval, overlain onto the seismic depth section.
405 An increase in basalt fraction within the gravity inversion, analogous to an increase in bulk
406 density of the SDR package, results in an increase in Moho depth.

407 As part of this analysis we converted our Moho depth results from the depth domain to the
408 time domain using a basement velocity of 6.31 km s^{-1}, corresponding to a basement density
409 of 2850 kg m^{-3} (Ludwig et al., 1970), in order to account for potential uncertainties in the
410 basement velocity model. Figure 7b shows Mohos calculated from the basalt fraction gravity
411 inversions overlain on the pre-stack time-migrated (PSTM) seismic profile together with both
412 shallow and deep seismic Moho candidates. Within the proximal domain the mismatch

between the gravity inversion Mohos and seismic Moho candidates is likely due to the presence of pre-rift sediments.

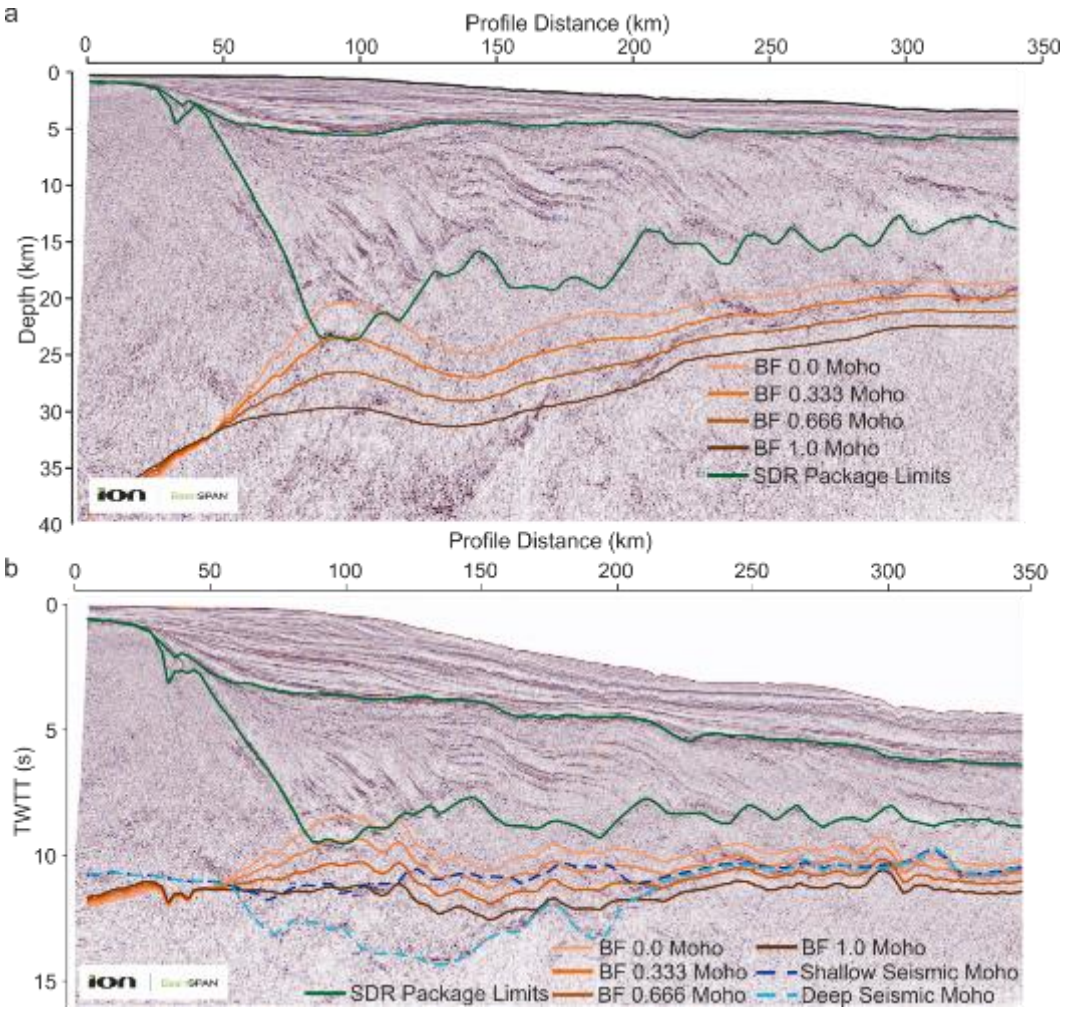

Figure 7. a) Basalt fraction gravity inversion Mohos overlain on PSDM seismic reflection profile. SDR package limits shown in green. b) Basalt fraction gravity inversion Mohos and seismic Mohos, converted into TWTT (6.31 km s^{-1} equivalent to 2850 kg m^{-3} basement density), overlain on PSTM seismic reflection profile with seismic Mohos. SDR package boundaries shown in green.

The shallow seismic Moho candidate lies within the range of the four Moho profiles calculated by the basalt-fraction gravity inversion. This is not the case with the deep seismic Moho candidate, which is too deep to match any of the basalt-fraction gravity inversion Mohos between a line-distance of 50 km and 210 km. Additionally, the deep seismic Moho candidate reaches a maximum TWTT of ~14 s (Fig. 7b), which is substantially beyond Warner's Moho guide of ~10 s TWTT (Warner, 1987). In addition, the joint inversion of gravity and seismic data (Section 4) using the deep seismic Moho candidate, gives unrealistic average

SDR and basement densities in excess of 3000 kg m^{-3}. As a consequence, the shallow seismic Moho candidate is more realistic and is our preferred seismic Moho interpretation, while the "deep seismic Moho candidate" is likely to be reflectivity from within the mantle, which we discuss further in Section 7.4.

An oceanwards traverse of the time-section (Fig. 7b) shows the shallow seismic Moho matches with different basalt-fraction gravity inversion Mohos along the section. At the proximal margin the shallow seismic Moho best fits with a high basalt fraction of 1.0, whereas at the distal margin the shallow seismic Moho best corresponds with a low basalt fraction of 0.333. This implies a changing lithological composition across the SDR package, where basalt fraction (bulk density) decreases oceanward.

6. Lateral variation in SDR package composition from basalt fraction and seismic observations

In order to interpret the composition of the SDR package in more detail we have combined our seismic observations with our basalt fraction results to determine if the composition varies laterally (Fig. 8). Based on the changing seismic character of the SDR package, alongside the potential lateral variation in basalt fraction, the SDR package can be split into three distinct sub-packages (Fig. 8a) that are roughly consistent with the sub-packages defined by McDermott et al. (2018). The first (oldest and innermost) sub-package consists of reflectors originating from a single source (in 2D) on the proximal margin. The second sub-package also shows reflectors originating from a single source on the proximal margin but extending across a larger horizontal distance (~150 km). The third sub-package has reflectors that progressively offlap one another in an eastwards direction. These sub-packages, interpreted initially from seismic character, are further delineated by quantifying the lateral variation in basalt fraction.

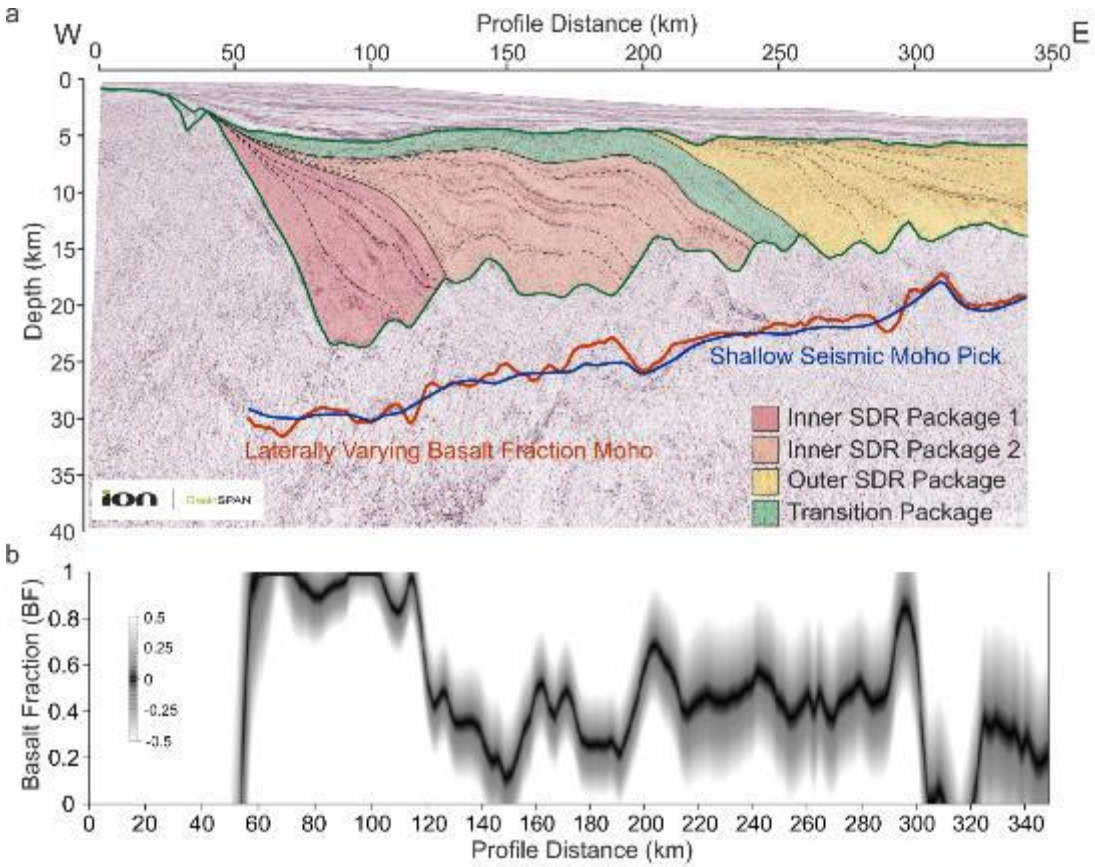

Figure 8. a) PSDM showing SDR boundaries (green), sub-package boundaries (solid black), SDR tracings (black, dashed), shallow seismic Moho (dark blue) and laterally varying basalt fraction Moho converted from the time domain (red) by assuming a basement density of 2850 kg m^{-3} and velocity of 6.31 km s^{-1}. b) Lateral variation in basalt fraction calculated by minimising the difference between the basalt fraction Mohos and the shallow seismic Moho in the time domain to avoid depth conversion uncertainties. Black is a difference of zero between the two Mohos, dark grey represents a misfit up to 0.25 s and white areas are a difference of 0.5 s and above.

The lateral variation in basalt fraction is calculated by minimising the difference between the shallow seismic Moho and basalt fraction Mohos in the time domain (Fig. 8b) assuming a constant basement density, giving the average basalt fraction of the SDR package at that point. The lateral variation in basalt fraction suggests the presence of three sub-packages within the SDR package, similar to the seismic observations. The first sub-package lies between a line-distance of 55 km and 115 km, with an average basalt fraction approaching 1.0. SDR reflector geometries show a single-point source at ~50 km before fanning out to form a growth wedge. The second sub-package lies immediately outboard of this, with its origin at ~60 km and notably thick flows between 115 km to 210 km, with an average basalt fraction of ~0.45. Within this package, reflectors appear to originate from a single point,

similar to inner SDR package 1, but reflectors are more laterally extensive, extending ~150km across the section. The third sub-package is located from ~210 km to the end of the profile and has an average basalt fraction of ~0.55. We have termed these packages, inner SDR package 1, inner SDR package 2 and outer SDR package respectively (Fig. 8a). Between inner SDR package 2 and the outer SDR package there is a seismic package that exhibits weak reflectivity and contains no reflectors representative of lava flows. This transitional package (Fig. 8a) marks a time gap between the inner and outer SDRs. Conversely, in the outer SDR package, reflectors progressively offlap towards the oceanic domain giving the appearance of lateral migration. Flows are mostly sub-parallel to each other with a slight thickening down dip, similar in appearance to SDRs described by Bodvarsson and Walker (1964). Overall the basalt fraction across the SDR package decreases oceanwards from a maximum of 1.0 in the west to ~0.2 in the east (Fig. 8b).

7. Discussion

Integration of the quantitative analysis, seismic observations and regional context enables us to infer the possible composition of the various SDR sub-packages, as well as the origin and the timing of each package relative to breakup (Fig. 9).

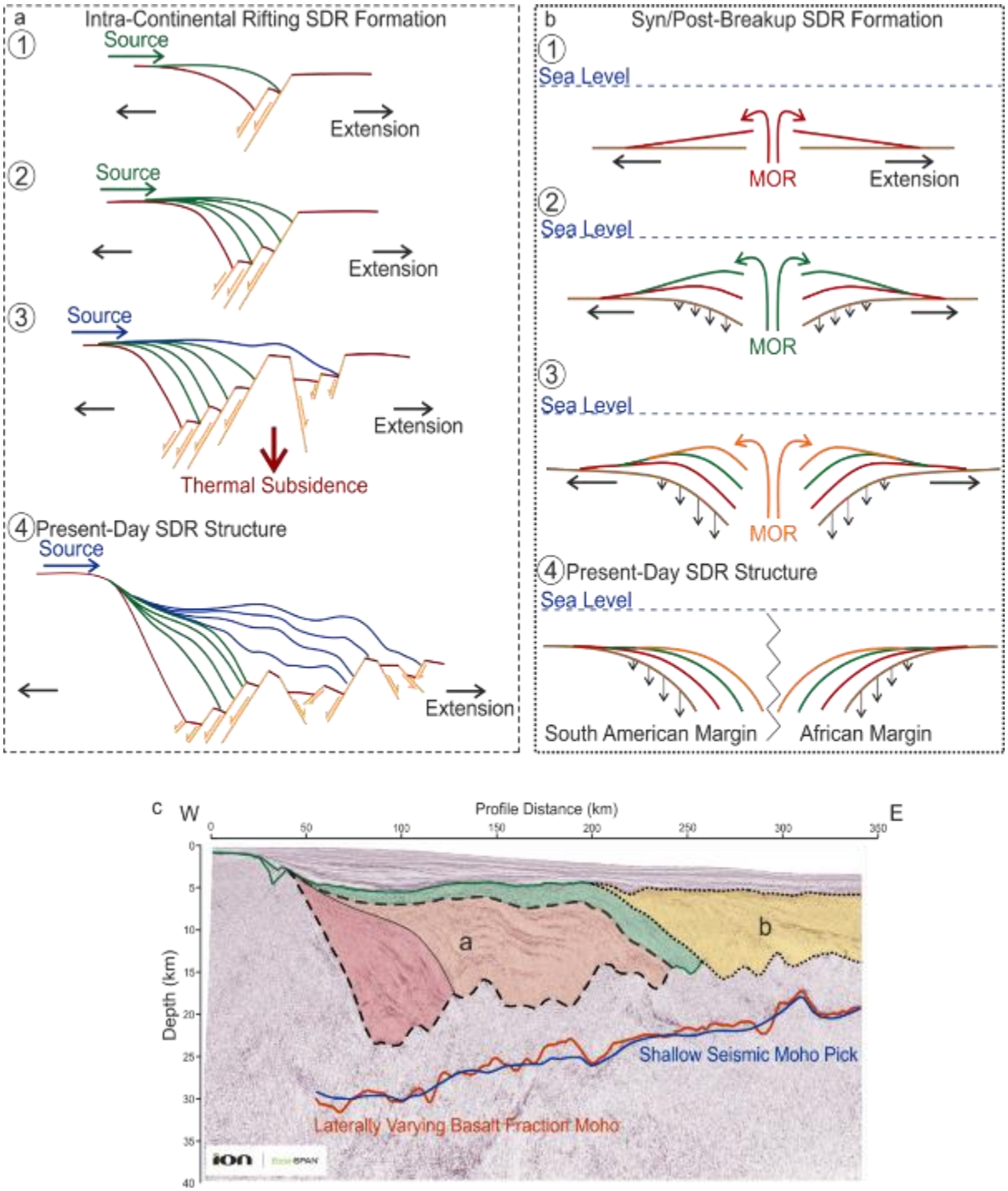

Figure 9. SDR formation models for SDR packages on the Pelotas rifted margin. a) Formation of intra-continental rifting SDRs (inner packages). 1) Half graben formation with first extrusive basalt flows infilling accommodation space. 2) Extension continues, and half-graben grows increasing accommodation space. Extrusive material continues to fill accommodation space. 3) Extension forms a horst and graben sequence increasing accommodation space. Thermal subsidence occurs, further increasing accommodation space above inner SDRs. b) Syn/post-breakup SDR formation (outer package). 1) Lava flows erupt below sea level from migrating Mid-Ocean Ridge (MOR). 2) MOR migrates due to sea-floor spreading, stopping flows travelling as far, resulting in progressive offlapping. Tectonic flexure from weight of lava flows begins. 3) Flows from MOR form high next to eruption source, with progressive offlapping continuing in the direction of divergence. 4) Present day SDR structure after tectonic and thermal subsidence has occurred. c) PSDM seismic reflection profile with SDR packages, shallow seismic Moho and laterally varying gravity inversion Moho. Intra-continental rifting SDRs denoted by dashed line (a) and post-breakup SDRs shown by dotted line (b).

472

7.1 Inner SDR package 1

Inner SDR package 1 (Fig. 7a) has the highest average basalt fraction (approaching 1.0) of the SDR sub-packages identified in this study. This suggests that its composition is 100% basaltic, possibly indicative of subaerial extrusive basaltic lava flows. Seismic reflectors within the package originate (in 2D) from a single-point source at the proximal limit of the package. Downwards termination of the reflectors occurs against a series of landward-dipping normal faults forming a horst and graben structure at the top of crystalline basement and a large amount of accommodation space. The lack of clear internal reflections within the underlying basement, which could be indicative of large magmatic intrusions, suggests that the SDRs are formed by an extrusive process instead of forming via feeder dykes within the basement. As no source is imaged within the seismic reflection data, it is most likely to be situated onshore. The seismic reflection profile is located in the only part of the Pelotas Basin where deposits from the Paraná LIP reach the coastline (Fig. 2a), implying a potential continuation of the onshore LIP volcanics offshore into the Pelotas Basin. The majority of the onshore Paraná LIP deposits consist of tholeiitic basalts which can range in density from 2700 kg m^{-3} to 2950 kg m^{-3} (Peate et al., 1992). With a basalt fraction of 1.0 (ρ_{mat}=2850 kg m^{-3}) it is therefore plausible that the dense material of inner SDR package 1 also comprises similar tholeiitic basalts. If inner SDR package 1 is composed of the same material as the erupting Paraná LIP then it is reasonable to assume that they formed contemporaneously, with lava flows from the Paraná extending eastwards into the available accommodation space within active rift basins resulting from extensional faulting. As the formation of the Paraná LIP itself is believed to be associated with regional extension (Hawkesworth et al., 2000), this contemporaneous eruption supports the conclusion from seismic observations that inner SDR package 1 was formed during intra-continental rifting prior to breakup (Fig. 9a). Formation of the inner SDRs would have started with the creation of accommodation space resulting from regional extension. The accommodation space would have then been filled by basalt flows from the Paraná LIP interbedded with eroded sediments.

7.2 Inner SDR package 2

Inner SDR package 2 (Fig. 7a) shows a sharp change in basalt fraction from inner SDR package 1, with an average basalt fraction of 0.45 indicating a higher proportion of less dense material, most probably sedimentary or volcano-sedimentary in origin. One possible source for this could be eroded material from the Paraná LIP interbedded with basalts still erupting from the onshore Paraná source. Alternatively, the entire package could consist of volcaniclastic sediments (rather than a mix of sediments and lavas) derived from the same active Paraná source as inner SDR package 1. Inner SDR package 2 is thought to have been contemporaneous with continued rift-related extension along normal faults, which formed additional horst and graben structures outboard of inner SDR package 1 and provided the accommodation space that was filled by an interbedded mix of eroded material and fresh basalts (Fig. 9a). As with inner SDR package 1, there are no significant intrusions visible on the seismic reflection profile, which might support a dyke-fed origin from directly below, rather than the preferred interpretation of a laterally-extrusive source to the west. Formation of both inner sets of SDRs would have been fault controlled, similar to the volcanic-faulting model (Buck et al., 2017), but with an extrusive, onshore source instead of a dyke-fed source. Conversely,

7.3 Outer SDR package

The outer SDR package (Fig. 7a) has an average basalt fraction of ~0.55 with individual reflectors extending for ~75-100 km. The individual layers within the SDR package thicken down-dip and offlap progressively to the east, suggesting a source from an eastwards-migrating ocean ridge (Palmason and Saemundsson, 1974), i.e. the newly formed Mid-Atlantic Ridge, which, at the time of outer SDR formation, would have been at an embryonic stage and located a short distance to the east of the profile (Fig. 9b). A migrating oceanic ridge typically produces MORB-type basalt with an average density of 2850 kg m^{-3} and a thickness of 7km (White et al., 1992). An average basalt fraction of 0.55 implies a bulk density within the SDR package of ~2700 kg m^{-3}. This could be indicative of a mix of basaltic (ρ=2850 kg m^{-3}) and volcaniclastic material, both sourced from the nearby ridge. In particular

it could be attributed to the presence of hyaloclastites that have a low density ranging from 2300-2700 kg m^{-3}, with an average density of 2500 kg m^{-3} (Moore, 2001). The presence of hyaloclastites interbedded within SDR flows was recorded on the southeast Greenland margin (Larsen and Saunders, 1998). Formation of hyaloclastites occurs in aquatic environments, where the eruption of magmatic material into water, or flowing laterally into water, results in instantaneous cooling and fragmentation (White et al., 2015). If hyaloclastites are present then this would mean that formation of the outer SDR package had to occur, at least in part, below sea-level, rather than entirely subaerially.

Flows within this package would have erupted from the embryonic Mid-Atlantic ridge, stacking on top of each other and causing a thickening of the flows closest to the spreading centre (Fig. 9b, Pindell et al., 2014 fig. 9f). Migration of the spreading centre would result in new flows offlapping the older flows in the direction of migration (Fig. 9b). Eruption from an embryonic Mid-Atlantic ridge implies syn-breakup formation of the outer SDR package.

7.4 Nature of the crustal basement, the deep reflector and the transition package

The techniques used within this study are not able to define the nature of the basement underlying the SDR package (continental, oceanic or transitional). Rather they provide constraints on the thickness and density of the basement, which can then be interpreted in terms of crustal type. Interpretations can also be made based on our understanding of the geometry and formation of the SDR package. If the inner SDR packages were formed by syn-rift volcanism this would imply the presence of underlying continental crust. Our gravity Moho indicates a maximum basement thickness of 10 km below the inner SDR packages, which has been defined as the upper limit of hyper-extended continental crustal thickness (Pérez-Gussinyé et al., 2006). This is consistent with the inner SDR packages forming on continental crust that has undergone extension and thinning during intra-continental rifting. The outer SDR package has been interpreted as syn-breakup, similar to SDRs described by Bodvarsson and Walker (1964) and others. Syn-breakup SDRs imply formation during, and perhaps immediately after, breakup meaning these SDRs must be emplaced over something other

than continental basement, possibly magmatic or transitional basement. The seismic reflection profile does not display typical Penrose oceanic crust properties (White et al., 1992), so we suggest that the outer SDR package has formed over transitional basement where continental crust has been heavily intruded by sills and dykes before transitioning eastwards into new oceanic basement.

The deep reflector visible on both PSTM and PSDM profiles (Figs. 3, 6, & 7) was initially interpreted as a possible seismic Moho (Fig. 3, Stica et al., 2014, fig. 7). We now consider it to be a possible reflection from within the mantle, below the actual Moho. In section 4.3.1, the deep reflector has been shown to be an unrealistic Moho candidate as it occurs at TWTTs approaching 14 s (Fig. 6). At line-distance ~210 km, however, the deep reflector joins the shallow seismic Moho, coincident with the location at which the inner SDR packages terminate. It is therefore possible that the deep reflector has a magmatic origin within the mantle and is related to the formation of the SDR packages.

The transition package (Fig. 7a), marks a time gap between the inner and outer SDR packages. No reflectivity indicative of SDR flows is visible within the package and reflectors marking the top of the package are discontinuous. The transition package thickens eastwards and pinches out towards the west, similar to the origin of both inner SDR packages. Stratigraphically, the transition package lies above inner SDR package 2 and is included within the basalt fraction calculation. This could affect the basalt fraction results for the sub-packages in particular inner SDR package 2. However, the discontinuous reflectors that depict the top of the package, alongside the geometry of the package can be interpreted as an extrusive lava flow which would be from the same source as the inner SDR packages. Composition of the transition package is therefore assumed to be similar to the inner packages.

8. Summary

Using bulk-density determined from gravity inversion and interpreted seismic characteristics the SDR package in the Pelotas Basin has been shown to contain two distinct sub-packages; the inner SDR package and the outer SDR package consistent with a previous study on the margin (McDermott et

al., 2018). The inner SDR package can be further divided into an inner SDR package 1 (older) and inner SDR package 2. Average basalt fraction results for each package are used as a proxy for composition, representing the proportional mix of basaltic and sedimentary/volcaniclastic material. Overall, the basalt fraction and vertically averaged density of the SDR package decreases oceanwards, consistent with a change from basaltic to volcaniclastic/sedimentary material oceanwards. Inner SDR package 1 is considered to consist entirely of extrusive basaltic material. Inner SDR package 2 is considered to consist of extrusive basaltic material with a high proportion of sedimentary/volcaniclastic material. The outer SDR package may contain a high proportion of volcaniclastics with subsidiary basaltic material.

The composition of each individual package, together with their regional context on the Atlantic margin, is used to infer the origin of the evolving SDR sequence (Fig. 9). The location of the seismic profile adjacent to the onshore LIP of the Paraná, the growth structures seen within the inner SDR packages and the horst-graben structure of top basement suggests the origin for the inner SDR packages is similar to the syn-rift origin of the onshore Paraná. The reflectors of the outer SDR package show progressive offlapping to the east and have an average basalt fraction of ~0.55. They are thought to have been sourced from an embryonic eastwards-migrating Mid Atlantic Ridge, lying immediately east of the profile at the time of their formation.

Finally, the timing of each package relative to breakup can be determined from the assumptions made about their origin. If the inner SDR packages are contemporaneous with the Paraná LIP and top basement displays horst-and-graben structures, then the inner SDRs would have formed during intra-continental rifting. In contrast, the outer SDR package, sourced from the embryonic Mid Atlantic ridge, will have formed during breakup and the initial stages of sea-floor spreading. Our results show that the SDRs imaged on the Pelotas profile record two different stages in the evolution of the South Atlantic margin, separated by the transitional package, from intra-continental rifting at the proximal margin through to breakup and subsequent sea-floor spreading at the distal margin. Symmetry of

598 SDRs over conjugate margins is only required after the formation of the transitional package, at which
599 time breakup began. The extraordinary SDRs presented in this study are a result of their positioning,
600 just offshore from the Paraná LIP, which has enabled the juxtaposition of the outer SDRs against the
601 inner SDRs that are otherwise absent on the margin along strike (Stica et al., 2014).

602 Our results, gathered from seismic observations and quantitative techniques, lead to the conclusion
603 that both mechanisms for SDR formation (Fig. 1) have operated in the Pelotas Basin (Fig. 9), indicating
604 that the two mechanisms are not exclusive of each other. Instead, we have shown that SDRs produced
605 by each mechanism were generated during different stages of continental rifting and breakup.
606 Classification of similar SDR sequences worldwide could help develop our overall understanding of the
607 evolution of magma rich margins.

608 ## References

609 Alvey, A., Gaina, C., Kusznir, N.J., Torsvik, T.H., 2008. Integrated crustal thickness mapping and plate
610 reconstructions for the high Arctic. Earth Planet. Sci. Lett. 274, 310–321.
611 https://doi.org/10.1016/j.epsl.2008.07.036

612 Alvey, A., Roberts, A., Kusznir, N.J., 2018. What is the thickness of the Earth's crust? Geoscientist.
613 https://doi.org/https://doi.org/10.1144/geosci2018-003

614 Athy, L.F., 1930. Density, porosity and compaction of sedimentary rocks. Am. Assoc. Pet. Geol. Bull.
615 14, 1–24.

616 Barton, A.J., White, R.S., 1997. Volcanism on the Rockall continental margin. J. Geol. Soc. London. 154,
617 531–536. https://doi.org/10.1144/gsjgs.154.3.0531

618 Birch, F., 1964. Density and composition of mantle and core. J. Geophys. Res. 69, 4377.
619 https://doi.org/10.1029/JZ069i020p04377

620 Blaich, O.A., Faleide, J.I., Tsikalas, F., Gordon, A.C., Mohriak, W.U., 2013. Crustal-scale architecture and
621 segmentation of the South Atlantic volcanic margin. Geol. Soc. London, Spec. Publ. 369, 167–

183. https://doi.org/10.1144/sp369.22

Bodvarsson, G., Walker, G.P.L., 1964. Crustal Drift in Iceland. Geophys. J. R. Astron. Soc. 8, 285–300.

Buck, W.R., 2017. The role of magmatic loads and rift jumps in generating seaward dipping reflectors on volcanic rifted margins. Earth Planet. Sci. Lett. 466, 62–69. https://doi.org/10.1016/j.epsl.2017.02.041

Carlson, R.L., Herrick, C.N., 1990. Densities and porosities in the oceanic crust and their variations with depth and age. J. Geophys. Res. 95, 9153. https://doi.org/10.1029/JB095iB06p09153

Chang, H.K., Kowsmann, R.O., Figueiredo, A.M.F., Bender, A.A., 1992. Tectonics and stratigraphy of the East Brazil Rift system: an overview. Tectonophysics 213, 97–138. https://doi.org/10.1016/0040-1951(92)90253-3

Chappell, A.R., Kusznir, N.J., 2008a. Three-dimensional gravity inversion for Moho depth at rifted continental margins incorporating a lithosphere thermal gravity anomaly correction. Geophys. J. Int. 174, 1–13. https://doi.org/10.1111/j.1365-246X.2008.03803.x

Chappell, A.R., Kusznir, N.J., 2008b. An algorithm to calculate the gravity anomaly of sedimentary basins with exponential density-depth relationships. Geophys. Prospect. 56, 249–258. https://doi.org/10.1111/j.1365-2478.2007.00674.x

Christensen, M.I., Mooney, W.D., 1995. Seismic velocity structure and composition of the continental crust - a global view. J. Geophys. Res. Earth 100, 9761–9788. https://doi.org/https://doi.org/10.1029/95JB00259

Cowie, L., Angelo, R.M., Kusznir, N.J., Manatschal, G., Horn, B., 2016. Structure of the ocean-continent transition, location of the continent-ocean boundary and magmatic type of the northern Angolan margin from integrated quantitative analysis of deep seismic reflection and gravity anomaly data. Geol. Soc. London, Spec. Publ. 438, 159–176. https://doi.org/10.1144/SP438.6

Cowie, L., Kusznir, N.J., Manatschal, G., 2015. Determining the COB location along the Iberian margin and Galicia Bank from gravity anomaly inversion, residual depth anomaly and subsidence analysis. Geophys. J. Int. 203, 1355–1372. https://doi.org/10.1093/gji/ggv367

Eldholm, O., Thiede, J., Taylor, A., 1987. Evolution of the Norwegian Continental margin - background and objectives. Proc. Ocean Drill. Program, Sci. Results 104, 5–25. https://doi.org/10.2973/odp.proc.ir.104.1987

Eldholm, O., Thiede, J., Taylor, E., 1989. Evolution of the Vøring Volcanic Margin. Proc. Ocean Drill. Program, 104 Sci. Results 104, 1033–1065. https://doi.org/10.2973/odp.proc.sr.104.191.1989

Fioravanti, C., 2014. Echoes of Separation. Pesqui. FAPESP 42–45.

Fitton, J.G., Larsen, L.M., Saunders, A.D., Hardarson, B.S., Kempton, P.D., 2000. Palaeogene continental to oceanic magmatism on the SE Greenland continental margin at 63°N: A review of the results of Ocean Drilling Program Legs 152 and 163. J. Petrol. 41, 951–966. https://doi.org/10.1093/petrology/41.7.951

Geoffroy, L., 2005. Volcanic passive margins. Comptes Rendus - Geosci. 337, 1395–1408. https://doi.org/10.1016/j.crte.2005.10.006

Geoffroy, L., Callot, J.-P., Scaillet, S., Skuce, A., Gelard, J.P., Ravilly, M., Angelier, J., Bonin, B., Cayet, C., Perrots, K., Lepvrier, C., 2001. Southeast Baffin volcanic margin and the North American-Greenland plate separation. Tectonics 20, 566–584. https://doi.org/https://doi.org/10.1029/2001tc900003

Gibson, I.L., Love, D., 1989. A Listric Fault Model for the Formation of the Dipping Reflectors Penetrated during the Drilling of Hole 642E, ODP Leg 104. Proc. Ocean Drill. Program, 104 Sci. Results. https://doi.org/10.2973/odp.proc.sr.104.195.1989

Gladczenko, T.P., Hinz, K., Eldholm, O., Meyer, H., Neben, S., Skogseid, J., 1997. South Atlantic volcanic margins. J. Geol. Soc. London. 154, 465–470. https://doi.org/10.1144/gsjgs.154.3.0465

669 Gozzard, S., Kusznir, N., Franke, D., Cullen, A., Reemst, P., Henstra, G., 2018. South China Sea crustal
670 thickness and oceanic lithosphere distribution from satellite gravity inversion. Pet. Geosci. 25,
671 112–128. https://doi.org/10.1144/petgeo2016-162

672 Graça, M., 2018. A formação da Elevação do Rio Grande e sua correlação com a evolução da Margem
673 Continental Sudeste Brasileira.

674 Gradstein, F.M., Agterberg, F.P., Ogg, J.G., Hardenbol, J., van Veen, P., Thierry, J., Huang, Z., 1994. A
675 Mesozoic Time-Scale. J. Geophys. Res. Earth 99, 24051–24074.
676 https://doi.org/10.1029/94JB01889

677 Greenhalgh, E.E., Kusznir, N.J., 2007. Evidence for thin oceanic crust on the extinct Aegir Ridge,
678 Norwegian Basin, NE atlantic derived from satellite gravity inversion. Geophys. Res. Lett. 34, 1–
679 5. https://doi.org/10.1029/2007GL029440

680 Harkin, C., Kusznir, N., Tugend, J., Manatschal, G., McDermott, K., 2019. Evaluating magmatic additions
681 at a magma-poor rifted margin: An East Indian case study. Geophys. J. Int. 25–40.
682 https://doi.org/10.1093/gji/ggz007

683 Hawkesworth, C.J., Gallagher, K., Kirstein, L., Mantovani, M.S.M., 2000. Tectonic controls on
684 magmatism associated with continental break-up : an example from the Paranà-Etendeka
685 Province. Earth Planet. Sci. Lett. 179, 335–349. https://doi.org/10.1016/S0012-821X(00)00114-
686 X

687 Hawkesworth, C.J.Y., Gallagher, K., Kelley, S., Mantovani, M., Peate, D.W., Regelous, M., Rogers, N.W.,
688 1992. Paraná magmatism and the opening of the South Atlantic. Geol. Soc. London, Spec. Publ.
689 Magmatism, 221–240. https://doi.org/https://doi.org/10.1144/gsl.sp.1992.068.01.14

690 Hinz, K., 1981. A Hypothesis on Terrestrial Catastrophes. Geol. Jahrb. R. E.

691 Hinz, K., Neben, S., Schreckenberger, B., Roeser, H.A., Block, M., Souza, K.G. De, Meyer, H., 1999. The
692 Argentine continental margin north of 48°S: Sedimentary successions, volcanic activity during

693 breakup. Mar. Pet. Geol. 16, 1–25. https://doi.org/10.1016/S0264-8172(98)00060-9

694 Janasi, V. de A., de Freitas, V.A., Heaman, L.H., 2011. The onset of flood basalt volcanism, Northern
695 Paran?? Basin, Brazil: A precise U-Pb baddeleyite/zircon age for a Chapec??-type dacite. Earth
696 Planet. Sci. Lett. 302, 147–153. https://doi.org/10.1016/j.epsl.2010.12.005

697 Jordan, T.H., Anderson, D.L., 1974. Earth Structure from Free Oscillations and Travel Times. Geophys.
698 J. R. Astron. Soc. 36, 411–459. https://doi.org/10.1111/j.1365-246X.1974.tb03648.x

699 Kusznir, N.J., Roberts, A.M., Alvey, A.D., 2018. Crustal structure of the conjugate Equatorial Atlantic
700 Margins , derived by gravity anomaly inversion. Geol. Soc. London, Spec. Publ. 476.
701 https://doi.org/https://doi.org/10.1144/SP476.5

702 Larsen, H.C., Saunders, A.D., 1998. Tectonism and volcanism at the southeast Greenland rifted margin:
703 a record of plume impact and later continental rupture. Proc. Ocean Drill. Progr. Sci. Results 152,
704 503–533. https://doi.org/10.2973/odp.proc.sr.152.1998

705 Lenoir, X., Féraud, G., Geoffroy, L., 2003. High-rate flexure of the East Greenland volcanic margin:
706 Constraints from 40Ar/39Ar dating of basaltic dykes. Earth Planet. Sci. Lett. 214, 515–528.
707 https://doi.org/10.1016/S0012-821X(03)00392-3

708 Ludwig, W.J., Nafe, J.E., Drake, C.L., 1970. Seismic Refraction, the Sea. Vol. 4 (Part 1).

709 McDermott, C., Lonergan, L., Collier, J.S., McDermott, K.G., Bellingham, P., 2018. Characterization of
710 Seaward-Dipping Reflectors Along the South American Atlantic Margin and Implications for
711 Continental Breakup. Tectonics 37, 3303–3327. https://doi.org/10.1029/2017TC004923

712 Mckenzie, D., Bickle, M.J., 1988. The volume and composition of melt generated by extension of the
713 lithosphere. J. Petrol. 29, 625–689. https://doi.org/https://doi.org/10.1093/petrology/29.3.625

714 Moore, J.G., 2001. Density of basalt core from Hilo drill hole, Hawaii. J. Volcanol. Geotherm. Res. 112,
715 221–230. https://doi.org/https://doi.org/10.1016/s0377-0273(01)00242-6

716 Morgan, R.L., Watts, A.B., 2018. Seismic and gravity constraints on flexural models for the origin of
717 seaward dipping reflectors. Geophys. J. Int. 214, 2073–2083.
718 https://doi.org/10.1093/GJI/GGY243

719 Müller, R.D., Roest, W.R., Royer, J.Y., Gahagan, L.M., Sclater, J.G., 1997. Digital isochrons of the world's
720 ocean floor. J. Geophys. Res. 102, 3211–3214. https://doi.org/10.1029/96JB01781

721 Mutter, J.C., Talwani, M., Stoffa, P.L., 1982. Origin of seaward-dipping reflectors in oceanic crust off
722 the Norwegian margin by subaerial sea-floor spreading. Geology 10, 353–357.
723 https://doi.org/10.1130/0091-7613(1982)10<353

724 Nayar, K.G., Sharqawy, M.H., Banchik, L.D., Lienhard, J.H., 2016. Thermophysical properties of
725 seawater: A review and new correlations that include pressure dependence. Desalination 390,
726 1–24. https://doi.org/10.1016/j.desal.2016.02.024

727 Palmason, G., 1973. Kinematics and Heat Flow in a Volcanic Rift Zone, with Application to Iceland.
728 Geophys. J. R. Astron. Soc. 33, 451–481. https://doi.org/10.1111/j.1365-246X.1973.tb02379.x

729 Palmason, G., Saemundsson, K., 1974. Iceland in Relation to the Mid-Atlantic Ridge. Annu. Rev. Earth
730 Planet. Sci. 2, 25–50. https://doi.org/10.1146/annurev.ea.02.050174.000325

731 Parker, R.L., 1972. The Rapid Calculation of Potential Anomalies. Geophys. J. R. Astron. Soc. 31, 447–
732 455. https://doi.org/https://doi.org/10.1111/j.1365-246x.1973.tb06513.x

733 Parons, L., Viereck, L., Love, D., Gibson, I., Morton, A., Hertogen, J., 1989. 22. The Petrology of the
734 Lower Series Volcanics, ODP Site 642. Proc. Ocean Drill. Program, Sci. Results 104.

735 Paton, D.A., Pindell, J., McDermott, K., Bellingham, P., Horn, B., 2017. Evolution of seaward-dipping
736 reflectors at the onset of oceanic crust formation at volcanic passive margins: Insights from the
737 South Atlantic. Geology 45, 439–442. https://doi.org/10.1130/G38706.1

738 Peate, D.W., Hawkesworth, C., Mantovani, M., 1992. Chemical stratigraphy of the Paraná lavas (South

America): Classification of magma types and their spatial distribution. Bull. Volcanol. 55, 119–139. https://doi.org/https://doi.org/10.1007/bf00301125

Pérez-Diaz, L., Eagles, G., 2014. Constraining South Atlantic growth with seafloor spreading data. Tectonics 33, 1848–1873. https://doi.org/10.1002/2014TC003644

Pérez-Gussinyé, M., Morgan, J.P., Reston, T.J., Ranero, C.R., 2006. The rift to drift transition at non-volcanic margins: Insights from numerical modelling. Earth Planet. Sci. Lett. 244, 458–473. https://doi.org/10.1016/j.epsl.2006.01.059

Pindell, J., Graham, R., Horn, B., 2014. Rapid outer marginal collapse at the rift to drift transition of passive margin evolution, with a Gulf of Mexico case study. Basin Res. 26, 701–725. https://doi.org/10.1111/bre.12059

Planke, S., Eldholm, O., 1994. Seismic response and construction of seaward dipping wedges of flood basalts: Voring volcanic margin. J. Geophys. Res. 99, 9263–9278. https://doi.org/10.1029/94JB00468

Quirk, D.G., Shakerley, A., Howe, M.J., 2014. A mechanism for construction of volcanic rifted margins during continental breakup. Geology 42, 1079–1082. https://doi.org/10.1130/G35974.1

Renne, P.R., Deckart, K., Ernesto, M., Feraud, G., Piccirillo, E.M., 1996. Age of the Ponta Grossa dike swarm (Brazil), and implications to Parana flood volcanism. Earth Planet. Sci. Lett. 144, 199–211. https://doi.org/10.1016/0012-821X(96)00155-0

Sandwell, D., Smith, W.H., 2009. Global marine gravity from retracked Geosat and ERS-1 altimetry: Ridge segmentation versus spreading rate. J. Geophys. Res. Solid Earth 114, 1–18. https://doi.org/10.1029/2008JB006008

Sclater, J.G., Christie, P.A.F., 1980. Continental stretching: An explanation of the Post-Mid-Cretaceous subsidence of the central North Sea Basin. J. Geophys. Res. Solid Earth 85, 3711–3739. https://doi.org/10.1029/JB085iB07p03711

763 Smith, R.A., 1961. A uniqueness theorem concerning gravity fields. Math. Proc. Cambridge Philos. Soc.
764 57, 865–870. https://doi.org/10.1017/S030500410003601X

765 Smith, W.H., Sandwell, D., 1997. Global Sea Floor Topography from Satellite Altimetry and Ship Depth
766 Soundings. Science (80-.). 277, 1956–1962. https://doi.org/10.1126/science.277.5334.1956

767 Steinberg, J., Roberts, A.M., Kusznir, N.J., Schafer, K., Karcz, Z., 2018. Crustal structure and post-rift
768 evolution of the Levant Basin. Mar. Pet. Geol. 96, 522–543.
769 https://doi.org/10.1016/j.marpetgeo.2018.05.006

770 Stica, J.M., Zalán, P.V., Ferrari, A.L., 2014. The evolution of rifting on the volcanic margin of the Pelotas
771 Basin and the contextualization of the Paraná-Etendeka LIP in the separation of Gondwana in the
772 South Atlantic. Mar. Pet. Geol. 50, 1–21. https://doi.org/10.1016/j.marpetgeo.2013.10.015

773 Talwani, M., Mutter, J.C., Eldholm, O., 1981. The initiation of opening of the Norwegian Sea. Oceanol.
774 Acta, Spec. Issue 23–30. https://doi.org/10.1136/bmj.b3136

775 Thiede, D.S., Vasconcelos, P.M., 2010. Paraná flood basalts: Rapid extrusion hypothesis confirmed by
776 new 40Ar/39Ar results. Geology 38, 747–750. https://doi.org/10.1130/G30919.1

777 Tugend, J., Gillard, M., Manatschal, G., Nirrengarten, M., Harkin, C.J., Epin, M.E., Sauter, D., Autin, J.,
778 Kusznir, N.J., McDermott, K., 2018. Reappraisal of the Magma-rich versus Magma-poor Rifted
779 Margin Archetypes. Geol. Soc. London, Spec. Publ.

780 Turner, S., Regelous, M., Kelley, S., Hawkesworth, C., Mantovani, M., 1994. Magmatism and
781 continental break-up in the South Atlantic: high precision 40Ar-39Ar geochronology. Earth
782 Planet. Sci. Lett. 121, 333–348. https://doi.org/10.1016/0012-821X(94)90076-0

783 Viereck, L.G., Hertogen, J., Parson, L.M., Morton, A.C., Love, D., Gibson, I.L., Hertogen, J., Parson, L.M.,
784 Love, D., Gibson, I.L., 1989. Chemical Stratigraphy and Petrology of the Voring Plateau Tholeiitic
785 Lavas and Interlayered Volcaniclastic Sediments at ODP Hole 624E. Proc. Ocean Drill. Program,
786 Sci. Results, Vol. 104 104, 367–396. https://doi.org/10.2973/odp.proc.sr.104.135.1989

787 Walker, G.P.L., 1960. Zeolite zones and dike distributions in relation to the structure of the basalts of
788 eastern iceland. J. Geol. 68, 515–528. https://doi.org/10.1086/626685

789 Walker, G.P.L., 1959. Geology of the Reydarfjördur area, Eastern Iceland. Q. J. Geol. Soc. 114, 367–
790 391. https://doi.org/https://doi.org/10.1144/gsjgs.114.1.0367

791 Warner, M.R., 1987. Seismic reflections from the Moho - the effect of isostasy. Geophys. J. R. Astron.
792 Soc. 88, 425–435. https://doi.org/10.1111/j.1365-246X.1987.tb06651.x

793 White, J.D.L., McPhie, J., Soule, S.A., 2015. Submarine Lavas and Hyaloclastite, Second Edi. ed, The
794 Encyclopedia of Volcanoes. Elsevier Inc. https://doi.org/10.1016/B978-0-12-385938-9.00019-5

795 White, R.S., McKenzie, D., 1989. Magmatism at rift zones: The generation of volcanic continental
796 margins and flood basalts. J. Geophys. Res. 94, 7685. https://doi.org/10.1029/JB094iB06p07685

797 White, R.S., McKenzie, D., O'Nions, R.K., 1992. Oceanic crustal thickness from seismic measurements
798 and rare earth element inversions. J. Geophys. Res. 97, 19683.
799 https://doi.org/10.1029/92JB01749

800 White, R.S., Smith, L.K., Roberts, A.W., Christie, P.F., Kusznir, N.J., Roberts, A.M., Healy, D., Spitzer, R.,
801 Chappell, A.R., Eccles, J.D., Fletcher, R., Hurst, N., Lunnon, Z., Parkin, C.J., Tymms, V.J., 2008.
802 Lower-crustal intrusion on the North Atlantic continental margin. Nature 452, 460–464.
803 https://doi.org/10.1038/nature06687

804